Journal of the Optical Society of America B
OPTICAL PHYSICS

Optical resonances in rotating dielectric microcavities of deformed shape

RAKTIM SARMA,[1] LI GE,[2,3] AND HUI CAO[1,*]

[1]Department of Applied Physics, Yale University, New Haven, Connecticut 06520-8482, USA
[2]Department of Engineering Science and Physics, College of Staten Island, CUNY, Staten Island, New York 10314, USA
[3]The Graduate Center, CUNY, New York, New York 10016, USA
*Corresponding author: hui.cao@yale.edu

Received 6 May 2015; revised 5 July 2015; accepted 5 July 2015; posted 6 July 2015 (Doc. ID 240389); published 27 July 2015

We investigate numerically rotation-induced changes of optical resonances in wavelength-scale dielectric cavities that are deformed from a circle. The relative change in the quality factor due to rotation is usually larger than that of the resonant frequency, even though both exhibit a threshold behavior, i.e., they barely change at low rotation speed. This threshold is increased at large deformation, which lowers the sensitivity to rotation. Presence of wave chaos can further increase the threshold for rotation-induced changes in resonant frequencies. Unlike the resonant frequency and quality factor, the change in far-field emission pattern by rotation does not display a threshold behavior, thus having a higher sensitivity at low rotation speed. The threshold behavior can be eliminated by designing the cavity shape with special symmetry, and the response of the far-field emission to rotation is also enhanced.

OCIS codes: (120.5790) Sagnac effect; (000.4430) Numerical approximation and analysis; (060.2800) Gyroscopes; (140.3945) Microcavities; (140.3948) Microcavity devices; (140.3370) Laser gyroscopes.

http://dx.doi.org/10.1364/JOSAB.32.001736

1. INTRODUCTION

Optical microcavities have been explored for various applications such as coherent light sources in integrated photonic circuits, single-photon emitters, and biochemical sensors [1,2]. One potential application that has received attention recently is an ultrasmall on-chip optical gyroscope [3–18]. Almost all conventional optical gyroscopes rely on the Sagnac effect for rotation sensing [9,11,19,20]. The Sagnac effect refers to rotation-induced phase shift between two counter-propagating waves in an optical loop. In a resonant cavity, the Sagnac effect causes frequency splitting between a pair of degenerate or quasi-degenerate modes. Since the Sagnac effect scales linearly with the cavity size [19,21], microcavities have much lower frequency response to rotation. As such, rotation-induced changes in other characteristics of microcavity resonances, such as the quality (Q) factor and the emission pattern, have been investigated in recent years [6,14,16–18].

Stationary microcavities with shape deformed from a circle have generated a lot of interest in the past two decades, with the quest to achieve optimal directional radiation from microlasers. Deformed microcavities also have been explored for rotation sensing, with the focus on rotation-induced changes in resonant frequencies of closed cavities [4,5,8,16,19]. Unfortunately, the shape deformation often lifts the frequency degeneracy of cavity modes, causing a threshold behavior for the rotation-induced change of the resonant frequencies. Recently, we proposed to use rotation-induced change in the emission directionality of an open deformed microcavity as a more sensitive measure of the rotation speed than that of the resonant frequency [17].

In this paper, we present a detailed numerical study on the effects of rotation on optical resonances in deformed microcavities with an open boundary. In particular, we investigate how the resonant frequencies, Q factors, and far-field emission patterns are modified by rotation in two-dimensional (2D) dielectric microcavities of various shapes. The Q factor, which determines the lasing threshold and the output power, is generally more sensitive to rotation than the resonant frequency. The wave chaos [22,23], which is common in deformed microcavities, increases the threshold for the rotation-induced change of the resonant frequencies. This threshold can be removed by designing the cavity shape to have degenerate stationary resonances. By investigating the dependence of rotation-induced far-field change on the cavity shape, we find the directional output from the deformed microcavities is a more sensitive signature of rotation. The cavity shape can actually be used as a parameter to tune the magnitude of the rotation-induced changes of cavity resonances.

Various methods have been developed to study photonic structures in a rotating frame [24–30]. In this work, we numerically calculate the cavity resonances using the finite-difference time-domain (FDTD) method and the scattering matrix method, which are adapted to the rotating frame. More details about these simulation methods can be found in [14,16,17]. Below, we consider a dielectric microdisk in free space; the disk thickness is much less than its radius, so it can be approximated as a 2D cavity with an effective index of refraction n. We present the results of the transverse magnetic (TM) resonances with the electric field perpendicular to the disk plane (parallel to the z axis) and the magnetic field parallel to the plane (the x–y plane). The disk rotates about the z axis in the counterclockwise direction with a constant angular velocity of rotation Ω. The rotation is slow enough that $\Omega R \ll c$, where R is the disk radius, and we keep only the leading-order terms of $\Omega R/c$ in the wave equation. In the rotating frame where the disk is stationary, the Maxwell equations retain their form, but the constitutive relations are modified [14,24,25,31].

In a stationary circular cavity, clockwise (CW) and counterclockwise (CCW) propagating waves do not couple, and they form two degenerate resonant modes of the cavity, which are characterized by the azimuthal number m and radial number l. The superposition of these two modes can form standing waves (with sine and cosine angular dependence), which are also resonant modes of the cavity. With rotation, the CW and CCW waves experience different refractive indices, and their frequencies start to split [4]. This frequency splitting is linearly proportional to the rotation velocity Ω. Since rotation makes the CW and CCW waves nondegenerate, the only resonances of a rotating circular cavity are the nondegenerate CW and CCW resonant modes.

In deformed stationary cavities, however, the CW and CCW waves may be coupled by scattering from the nonisotropic cavity boundary, and they form two quasi-degenerate resonances of frequency splitting Δk_0. With rotation, the frequency difference between these two quasi-degenerate resonances can be written as [4]

$$\Delta k_r(\Omega) = \left[\Delta k_0^2 + \left(\frac{g}{c}\Omega\right)^2\right]^{\frac{1}{2}}, \tag{1}$$

where g is a coupling constant that is proportional to the size of the cavity. Only when the rotation velocity Ω exceeds a certain threshold value $\Omega_c = c\Delta k_0/g$, the rotation-induced frequency shift $g\Omega/c$ becomes comparable with the intrinsic splitting Δk_0. For $\Omega < \Omega_c$, Δk_r is approximately equal to Δk_0 and is barely changed by rotation. Hence, there exists a "dead zone" at low rotation speed for the rotation-induced change of the resonant frequencies. Once the rotation-induced frequency shift is much larger than the intrinsic splitting, Δk_r approaches its asymptote $g\Omega/c$ and increases linearly with the rotation speed. Nonmonotonic behavior of the frequency splitting is also possible due to rotation-induced mode coupling in open microcavities [16]. The threshold rotation speed, Ω_c, usually decreases with the cavity size, as intrinsic splitting, Δk_0, reduces exponentially with the cavity size, whereas g increases linearly [32].

2. ELLIPTICAL CAVITIES

In this section, we begin with a simple deformed cavity shape, the ellipse [32–37], as drawn in Fig. 1(a). In Cartesian coordinates, the cavity boundary is given by $(x/a)^2 + (y/b)^2 = 1$, where $2a$ and $2b$ are the lengths of the minor and major axes, respectively ($a < b$). We vary the ratio a/b, while keeping the area πab constant. For the results presented below, we set $R = \sqrt{ab} = 0.54$ μm, and the wavelength (in vacuum) λ is around 0.72 μm. The refractive index is equal to 3.0 inside the cavity and 1.0 outside. For a/b close to 1, the high-Q modes resemble the whispering-gallery (WG) modes in a circular disk, and they each can be assigned a dominant azimuthal number m and a radial number l. The coupling between CW and CCW waves in the ellipse results in a frequency splitting Δk_0. The quasi-degenerate pair of modes have even and odd symmetry with respect to the major or minor axes, as seen in an example given in Figs. 1(b) and 1(c).

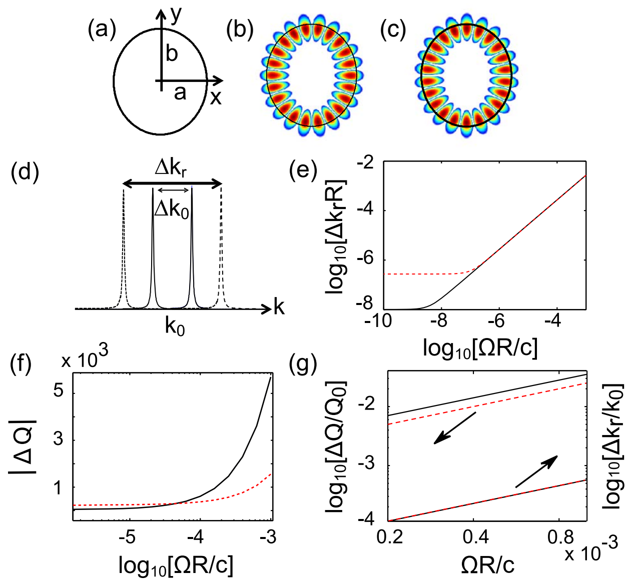

Fig. 1. Rotation-induced changes in the resonances of elliptical cavities. (a) A 2D microcavity of elliptical shape. The lengths of the minor and major axes are $2a$ and $2b$, respectively. The deformation is characterized by the ratio $a/b < 1$. (b) and (c) Spatial distribution of the electric field magnitude ($|E_z|$) for a pair of quasi-degenerate modes in the elliptical cavity with $a/b = 0.88$ and refractive index $n = 3.0$. The two modes, resembling the whispering-gallery modes in a circular cavity, are characterized by the dominant azimuthal number $m = 11$ and radial number $l = 1$. They possess even and odd symmetry with respect to the minor axis (x axis). (d) Schematic showing the frequency splitting Δk_0 of a quasi-degenerate pair of modes (solid lines) in an elliptical cavity without rotation, and the frequency splitting Δk_r with rotation. The higher-frequency (lower-frequency) mode of the quasi-degenerate pair is blueshifted (red) by rotation (dashed lines). (e) Normalized frequency shift $\Delta k_r R$ as a function of the normalized rotation speed $\Omega R/c$ for a pair of quasi-degenerate modes with $m = 11$ and $l = 1$ in the ellipse with $a/b = 0.88$ (red dashed line) and 0.92 (black solid line). Their normalized frequencies are approximately the same, $kR \simeq 4.73$, where $k = 2\pi/\lambda$ and $R = \sqrt{ab}$ is the average radius of the cavity. (f) Magnitude of rotation-induced changes in Q, $|\Delta Q|$, for the same pair of modes in (b). Black solid line and red dashed line correspond to $a/b = 0.92$ and 0.88, respectively. (g) Relative changes in the resonant frequency $\Delta k_r/k_0$ and the quality factor $\Delta Q/Q_0$ for the corresponding modes in (e) and (f). The vertical axis is shown in log scale to demonstrate the difference in magnitude between $\Delta k_r/k_0$ and $\Delta Q/Q_0$.

The stronger the deformation, i.e., the smaller the ratio a/b, the larger the splitting Δk_0.

When the ellipse rotates, the higher-frequency mode of the quasi-degenerate pair is blueshifted, and the lower-frequency one is redshifted [Fig. 1(d)]. We numerically calculate the frequency splitting Δk_r in the rotating ellipse using the FDTD method. A spatial grid size of 4 nm is used, and each time step is 6.6×10^{-18} s. The simulation is run typically for 20×10^6 time steps to resolve the frequency shift by rotation. At very low rotation speed, the frequency shift is so small that extremely long running time is required. In such a case, we resort to the scattering matrix approach. Figure 1(e) plots the value of Δk_r as a function of rotation speed Ω for a pair of quasi-degenerate modes with $m = 11$ and $l = 1$ in the ellipse with $a/b = 0.88$ (dashed line) and 0.92 (solid line). Their normalized frequencies are approximately the same, $kR \simeq 4.73$, where $k = 2\pi/\lambda$ and $R = \sqrt{ab}$ is the average radius of the cavity. The threshold values, expressed as $\Omega_c R/c$, are on the order of $\sim 10^{-7}$ and $\sim 10^{-9}$ for the ellipses with $a/b = 0.88$ and 0.92, respectively, below which the frequency spacing of the two resonances remains nearly unchanged from Δk_0. Thus, the larger deformation leads to a wider dead zone. For $\Omega > \Omega_c$, Δk_r increases linearly with Ω in both cavities, as it is dominated by rotation-induced frequency splitting.

The cavity shape deformation also causes a dead zone in the rotation-induced change of Q, as shown in Fig. 1(f). The quasi-degenerate pair of resonances have slightly different Q even at $\Omega = 0$. For $\Omega \gg \Omega_c$, the Q for one mode increases with Ω and decreases for the other. The magnitude of the change in Q due to rotation, $|\Delta Q|$, is the same for the pair (to the leading order of $R\Omega/c$ [16]). The larger the deformation (smaller a/b), the wider the dead zone for $|\Delta Q|$. Beyond the dead zone, the larger slope of $|\Delta Q|$ versus Ω for a smaller value of a/b indicates the cavity with weaker deformation is more responsive to rotation.

In Fig. 1(g), we compare the relative changes in resonant frequency and Q factor due to rotation, i.e., $\Delta k_r/k_0$ and $\Delta Q/Q_0$, where k_0 and Q_0 are the average frequency and quality factor for the quasi-degenerate pair of modes at $\Omega = 0$. $\Delta Q/Q_0$ is more than one order of magnitude higher than $\Delta k_r/k_0$, indicating the relative change of Q by rotation is much larger than that of frequency in the wavelength-scale elliptical cavity.

Next, we investigate the rotation-induced changes in the output intensity patterns of elliptical cavities with the FDTD method. As the radius of curvature varies along the cavity boundary, the strongest emission occurs at the locations of the highest curvature. The main emission directions for the elliptical cavities are therefore parallel to the minor axis of the ellipse (x axis, $\theta = 0°$, 180°). As shown in Fig. 2(a), the far-field intensity patterns for a stationary quasi-degenerate pair of modes have even and odd parity with respect to the major and minor axes of the ellipse, and there are several lobes around $\theta = 0°$, 180° as a result of the interference of the emission from CW and CCW waves in the cavity. By decomposing the field outside the cavity into CW and CCW wave components, we identify the far-field patterns for CW and CCW waves [Fig. 2(b)]. The CW and CCW in the stationary resonances do not emit exactly in the same directions, even though they

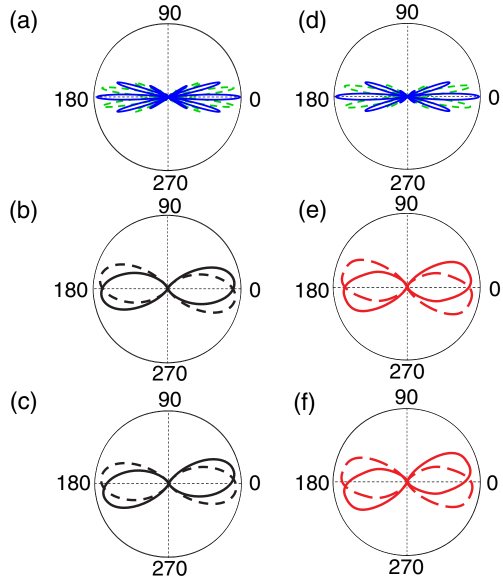

Fig. 2. Evolution of far-field emission patterns of elliptical microcavities with rotation. The deformation of the ellipse is $a/b = 0.92$ in (a)–(c) and 0.88 in (d)–(f). (a) and (d) Angular distribution of far-field intensity $I(\theta)$ (at $r = 50R$) of quasi-degenerate pairs of modes shown in Fig. 1 at $\Omega R/c = 0$. The blue solid (green dashed) curve represents the mode with even (odd) symmetry with respect to the x axis. (b) and (e) Angular distribution of far-field intensity for the CW and CCW wave components in the stationary resonances shown in (a) and (d). The solid (dashed) curve represents the CW (CCW). The output directions of CW and CCW waves are symmetric with respect to the horizontal axis. (c) and (f) Angular distribution of far-field intensity $I(\theta)$ (at $r = 50R$) of the modes in (a) and (d) at $\Omega R/c = 10^{-4}$. The interference fringes in the output intensity patterns of stationary cavity (a) and (d) vanishes, as the modes evolve from standing wave to traveling wave with rotation. The emission patterns of the two traveling-wave modes at high rotation speed are not symmetric with respect to the horizontal axis.

are symmetrical about the major and minor axes. This difference is caused by wave effects, including the Goos–Hänchen shift and Fresnel filtering, which become significant in the wavelength-scale cavities [38–41].

With increasing rotation speed, the standing-wave modes evolve to CW and CCW traveling-wave resonances, and the interference fringes in the far-field patterns vanish in Fig. 2(c). Moreover, output directions for CW and CCW waves are no longer symmetric with respect to the major and minor axes, as both rotate slightly in the direction of rotation (CCW). This behavior is attributed to the rotation-induced change in the refractive index, namely, the index increases with for the co-propagating wave (propagating in the same direction as the rotation) and decreases for the counterpropagating wave. In the elliptical cavity with smaller a/b, the difference between the CW and CCW output directions at $\Omega = 0$ is larger, and the rotation-induced change in the far-field pattern is smaller [Figs. 2(d)–2(f)].

To quantify the far-field change by rotation, we compute using the scattering matrix method, $\Delta_I(\Omega) \equiv \int |I_\Omega(\theta) - I_0(\theta)|^2 d\theta$, where $I_\Omega(\theta)$ $(I_0(\theta))$ represents the angular

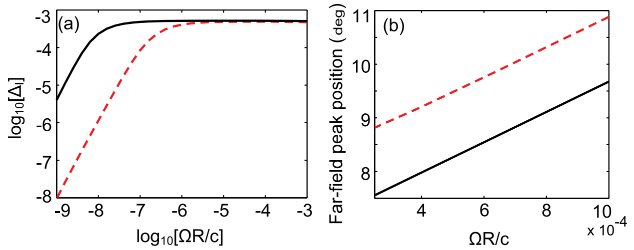

Fig. 3. Quantitative changes in the emission patterns of elliptical cavities by rotation. (a) Rotation-induced change in the far-field intensity pattern $I(\theta)$ as a function of the normalized rotation speed $\Omega R/c$ for the blueshifted modes. The black solid (red dashed) line corresponds to the mode in the elliptical cavity with $a/b = 0.92$ (0.88). (b) Polar angle for a major emission peak of the CW-wave-dominant mode increases with rotation. Black solid black (red dashed) line corresponds to the ellipse with $a/b = 0.92$ (0.88).

distribution of far-field intensity at rotation speed Ω (without rotation, $\Omega = 0$), normalized by $\int I_\Omega(\theta)\mathrm{d}\theta = \int I_0(\theta)\mathrm{d}\theta = 1$. Figure 3(a) is a logarithmic plot of Δ_I versus Ω for the higher-frequency mode of the quasi-degenerate pair in Fig. 1. As Ω increases, Δ_I does not exhibit a threshold behavior: it changes linearly with the rotation speed inside the dead zone of rotation-induced change of the resonant frequencies.

This is because, even within the dead zone, the balance between the CW and CCW wave components in the cavity resonance is already broken by rotation; such imbalance, albeit weak, modifies the interference between the CW and CCW waves and causes a notable change in the far-field pattern [17]. At low rotation speed, Δ_I increases rapidly with Ω and then tapers off once Ω exceeds Ω_c, as the resonances already become CW and CCW dominated and their far-field patterns barely change further, except for a gradual rotation of the intensity patterns in the direction of rotation as mentioned above. Since the interference vanishes much faster in the cavity with smaller deformation ($a/b = 0.92$), the magnitude of Δ_I at low rotation speed is orders of magnitude larger when compared with the cavity with larger deformation ($a/b = 0.88$). Figure 3(b) plots the polar angle of a far-field emission peak for the CW-dominant mode at high rotation speed, and it increases linearly with Ω. The other emission peak moves in the same direction at the same speed.

Here, we have presented only the results for the higher-frequency mode of the quasi-degenerate pair; the lower-frequency mode is redshifted by rotation and the magnitude of change is the same as that for the higher-frequency mode.

3. QUADRUPLE CAVITY

While the elliptical cavity has integrable ray motion, many deformed cavities support partially or fully chaotic ray dynamics. Harayama *et al.* studied the rotation-induced change of the resonant frequencies in a rotating chaotic microcavity with a closed boundary [5]. In this section, we investigate how wave chaos modifies the optical resonances of an open chaotic microcavity in the rotating frame. To isolate the effects of wave chaos, we compare a similarly deformed quadruple cavity and elliptical cavity, with chaotic ray dynamics supported only by the former [23]. The cavity boundary of a quadruple cavity is described by $r = R[1 + \epsilon \sin(2\theta)]$ in the polar coordinates, where R is the average radius and ϵ is the deformation parameter. When ϵ is small, it is nearly impossible to distinguish a quadruple cavity and an elliptical cavity by eye, as Fig. 4(a) shows. This is because an ellipse is approximately

$$r(\theta) \approx \frac{\sqrt{2}b}{\sqrt{2-F}}\left[1 + \frac{F}{4-2F}\sin(2\theta)\right] \quad \textbf{(2)}$$

to the leading order of $F = 1 - (a/b)^2$.

It requires an extremely fine spatial grid in the numerical simulation to capture the tiny difference in the shape of cavity boundary; hence, the results presented in this section are obtained by the scattering matrix method [17], which does not rely on spatial discretization [16,17].

Since the elliptical cavity is integrable while the quadruple is not, Kolmogorov–Arnold–Moser (KAM) transition [22] only occurs in the latter. Figures 4(b) and 4(c) shows the Póincare surface of section (SOS) [42,43] for the elliptical and quadruple cavities. The SOS displays phase space trajectories as points in a 2D plot with coordinates θ and $\sin\chi$, where θ is the azimuthal angle for the point on the cavity boundary, and χ is the incident angle at the cavity boundary. The red dashed lines mark the critical angle for total internal reflection.

The SOS of the quadruple cavity in Fig. 4(c) exhibits a mixed phase space (partially regular and partially chaotic) with islands that correspond to quasi-periodic orbits around stable fixed points. Nevertheless, there still exist continuous KAM curves in the Póincare surface of section in the region of large incident angles in a quadruple cavity, due to regular ray motions similar to those in an ellipse [Fig. 4(b)]. These KAM curves represent WG modes in both cavities [Figs. 5(a) and 5(b)], and one would expect these modes to behave similarly upon the rotation of the cavity.

The above discussion, however, does not take into account wave tunneling effects. There are two tunneling processes: one is the tunneling between CW and CCW waves in a stationary resonance; the other is the tunneling from the inside of the

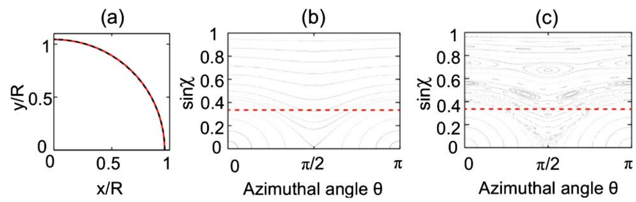

Fig. 4. Comparison of a chaotic cavity to a nonchaotic one with a similar boundary. (a) Boundaries of an ellipse cavity with $a/b = 0.92$ and $ab = R^2$ (black dashed line) and a quadruple cavity of $r(\theta) = R[1 + 0.044 \sin(2\theta)]$ (red line) in the first quadrant, which almost overlap. (b) Poincaré surface of section of the elliptical cavity consisting only of KAM curves, due to the integrable ray motion. Only the section for $\theta \in [0, \pi]$ and $\sin\chi > 0$ is shown; the rest can be obtained by symmetry operation. Red dashed lines mark the critical angle at $\sin\chi = 1/n$. (c) Poincaré surface of section (SOS) of the quadruple cavity consisting of KAM curves, islands, and chaotic regions, reflecting the partially chaotic ray dynamics. The horizontal coordinate θ is the azimuthal angle for the point on the cavity boundary; the vertical coordinate is $\sin\chi$, and χ is the incident angle at the cavity boundary.

cavity to the outside, which leads to emission. In an ellipse, the above tunneling processes for a WG-type mode can only be realized via direct tunneling, which has to overcome the wide separation of the KAM curves with opposite sin χ in the SOS or that from the KAM curve to the leaky region below the critical line for total internal reflection. In a quadruple, however, the presence of chaotic regions in the SOS enables the chaos-assisted tunneling, which is a combination of tunneling over a short distance from the KAM curve to the neighboring chaotic region and the chaotic diffusion to the leaky region [44,45].

The chaos-assisted tunneling increases the splitting of quasi-degenerate modes at $\Omega = 0$ [46,47]. Consequently, the quadruple cavity has a much larger dead zone compared with the similarly deformed elliptical cavity, as shown in Fig. 5(c). Beyond the dead zone, the frequency splitting, determined by the azimuthal number m, becomes similar for these two pairs of resonances.

Next, we examine the far-field emission from the rotating quadruple cavity. As shown in Fig. 5(d), the output directions of the CW and CCW wave components in the stationary resonances slightly deviate from 0°, 180°. This is similar to the elliptical cavity [Fig. 5(e)], but the deviation is larger in the quadruple cavity. The rotation-induced change in far-field

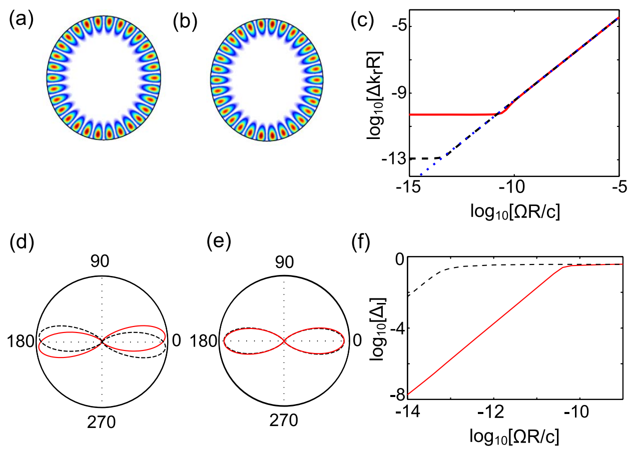

Fig. 5. Rotation-induced changes in the resonances of a quadruple cavity, which are compared with those of an elliptical cavity shown in Fig. 4. The cavity radius is $R = 1.5$ μm, and the resonance wavelength (in vacuum) is $\lambda \sim 1.5$ μm. (a) and (b) The spatial distribution of field intensity of the even-parity resonance about the horizontal axis in the (a) quadruple cavity and the (b) elliptical cavity. The refractive index is $n = 3.0$ inside the cavity and 1.0 outside. The modes are WG-like, with the radial number $l = 1$ and the dominant azimuthal number $m = 15$. (c) Frequency splitting $\Delta k_r R$ as a function of the normalized rotation speed $\Omega R/c$ for the two modes in (a) and (b). Black dashed line and red solid line show the resonances in the ellipse and quadruple, respectively. Blue dotted line shows the frequency splitting $\Delta k_r R$ of resonances with the same radial number and azimuthal number in a circular cavity with the same refractive index and similar radius. (d) and (e) Angular dependence of the far-field intensity for the CW (red solid line) and CCW (black dashed line) wave components in the resonances shown in (a) and (b) of the (d) stationary quadruple cavity and (e) elliptical cavity. (f) Plot of the rotation-induced change in far-field intensity pattern Δ_I versus the normalized rotation speed $\Omega R/c$ for the modes in (a) and (d) (red solid line) and (b) and (e) (black dashed line).

intensity pattern Δ_I exhibits the same trend, as discussed in the previous section. Since the dead zone is much wider in the quadruple due to wave chaos, the change in the far-field intensity pattern by rotation is much smaller than in the elliptical cavity at low rotation speed [Fig. 5(f)].

4. DEFORMED CAVITIES WITH DEGENERATE MODES

The resonances of the deformed microcavities studied above are already nondegenerate at rest, causing a dead zone for the rotation-induced change of the resonant frequencies. To eliminate the dead zone, Sunada and co-workers chose the cavities with special symmetry such as D_ν [4,5].

A special example is the dihedral group of $\nu = 3$, referred to the D_3 cavity, which has the same rotation and reflection symmetries as an equilateral triangle. The cavity boundary is defined in the polar coordinates by $r(\theta) = R[1 + \epsilon \cos(3\theta)]$, where R is the radius and ϵ is the deformation parameter. Such a cavity supports degenerate resonances at $\Omega = 0$ if their wavefunctions do not possess simultaneous rotation and reflection symmetries or, in other words, the azimuthal numbers of these resonances are not integer multiples of 3. As a result of this degeneracy, the rotation-induced change of the resonant frequencies has no dead zone for such resonances. The previous studies of Sunada *et al.*, however, are limited to the closed cavities. In this section, we investigate the open D_3 cavity and track the changes in resonant frequency, Q factor, and emission pattern due to rotation. Because a small perturbation of the boundary of the cavity (for example, finite grid size used in FDTD simulation) could lift the degeneracy, the calculations in this section were done using the scattering matrix method.

With small deformation, the ray dynamics in the D_3 cavity is partially chaotic. The Poincaré surface of section has continuous KAM curves that support high-Q WG modes. In Fig. 6, we compare a degenerate pair of WG modes with the dominant azimuthal number $m = 16$ in two D_3 cavities of different deformations $\epsilon = 0.015, 0.025$. The cavity radius is $R = 1.6$ μm and $\lambda \sim 1.5$ μm. Thanks to the degeneracy, each of the pair can be represented by a CW or CCW traveling wave only and has a smooth intensity distribution along the cavity boundary [Figs. 6(a) and 6(b)]. Figure 6(c) plots the frequency difference of the pair, which increases linearly with the rotation speed.

Although the magnitude of the frequency splitting is similar for the two deformations, the rotation-induced change in Q is very different, as seen in Fig. 6(d). The cavity of the smaller ϵ has a higher Q at rest, and the Q change by rotation is larger by more than one order of magnitude. The two degenerate CW and CCW resonances in the stationary D_3 cavity have the distinct far-field patterns, as shown in Fig. 7(a) for $\epsilon = 0.015$. At high rotation speed, the emission peak positions shift due to rotation [Fig. 7(b)]. The rates of shifts, given by the slope of peak position versus Ω in Fig. 7(b), are comparable for the deformations $\epsilon = 0.015, 0.025$. This is expected because the modes of both cavities have the same dominant m.

Although an ideal D_3 cavity is free of a dead zone, in reality the boundary defect and roughness, generated unintentionally during the fabrication processes, cause the coupling between CW and CCW waves, lifting the frequency degeneracy of

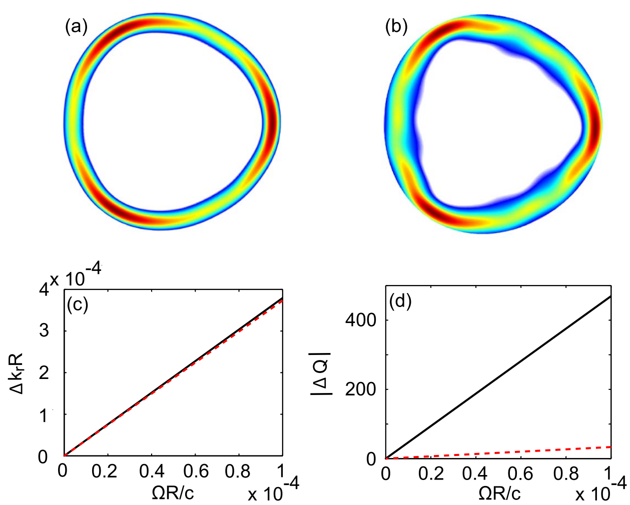

Fig. 6. Effects of rotation on a pair of degenerate WG modes with the radial number $l = 1$ and the dominant $m = \pm 16$ in two D_3 cavities of same radius ($kR \simeq 6.62$) and refractive index ($n = 3.0$) but different deformations ($\epsilon = 0.015,\ 0.025$). (a) and (b) Intensity distribution of the CW wave mode of the degenerate pair with (a) $\epsilon = 0.015$ and (b) 0.025. The degenerate CW and CCW resonances can be linearly superposed to create eigenstates, which are even and odd about the symmetry axes. (c) Frequency difference of the pair as a function of the normalized rotation speed $\Omega R/c$. The black solid line is for $\epsilon = 0.015$, and the red dashed line is for $\epsilon = 0.025$; a slight difference is observed for the two deformations. (d) Rotation-induced change in Q versus $\Omega R/c$. The cavity of $\epsilon = 0.015$ (black solid line) has a larger $|\Delta Q|$ than the one with $\epsilon = 0.025$ (red dashed line).

the resonances at rest and creating a dead zone. In context to microcavities, in general it is known that disorder, or any random superposition of high-order harmonic perturbations, leads to a splitting of the resonances at rest. Compared with the circular cavity, the D_3 cavity is more robust against the boundary imperfections because its mode intensity maximizes only at three localizations on the boundary [Figs. 6(a) and 6(b)] instead of uniformly distributed across the entire boundary as a WG mode of a circular cavity. One possible way to further reduce the size of the dead zone and thus increase the sensitivity to rotation is using single crystalline cavities that can be grown by epitaxy methods and have atomic-flat surfaces. One such candidate is hexagon cavities, which belong to a higher symmetry group ($\nu = 6$) and also support degenerate modes.

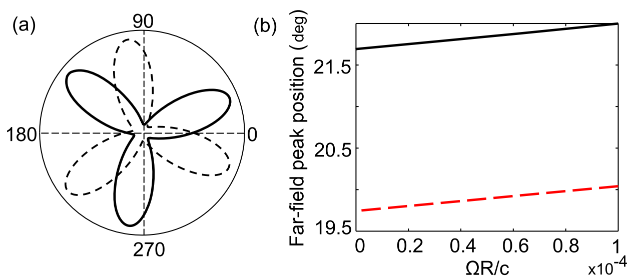

Fig. 7. Rotation-induced changes in the far-field emission patterns for a pair of degenerate resonances of the D_3 cavities shown in Fig. 6. (a) Angular distribution of the far-field intensities of the degenerate CW (solid line) and CCW (dashed line) resonances in the D_3 cavity of $\epsilon = 0.015$ at rest. (b) Rotation-induced change of a major emission peak position versus $\Omega R/c$ for the degenerate modes in Fig. 6. Black solid and red dashed lines show the emission peak of the CW wave mode in the first quadrant for $\epsilon = 0.015,\ 0.025$, respectively.

5. CONCLUSION

To conclude, we studied rotation-induced changes in the resonances of wavelength-scale dielectric microcavities of different shape deformations. In elliptical cavities, the rotation-induced frequency shifts, and Q changes show a threshold behavior below a certain value of rotation speed in which the changes are negligible. Increasing the deformation raises the threshold value and, hence, lowers the responses to rotation. Above the threshold value, both frequency and Q factor of the modes change linearly as a function of rotation speed, and the relative changes in Q are larger than the relative changes in resonant frequency. Unlike the resonant frequency and Q, the change in far-field emission pattern by rotation does not show a threshold behavior, thus exhibiting higher sensitivity to rotation at low rotation speed. The magnitude of rotation-induced changes is modified by the presence of wave chaos in deformed microcavities such as a quadruple cavity. Wave chaos increases the frequency splitting and reduces the sensitivity of the resonances to rotation especially at low rotation speed. Hence, the resonant modes of a quadruple cavity exhibit smaller changes by rotation than those in the elliptical cavity, which has a nearly overlapping boundary. We believe that this conclusion is general, i.e., for all nonintegrable geometries the dead zone should be larger compared with their integrable correspondence. Finally, we also studied microcavities that possess special symmetry and support degenerate modes, e.g., the D_3 cavity. Although the Q factors of the resonances of these cavities are relatively low, the rotation-induced changes of frequencies and Qs of the modes are free of any threshold behavior and the far-field intensity is highly sensitive to rotation. In addition to the deterministic cavity geometries, the structural disorder introduced due to fabrication inaccuracies could have a significant impact on the rotation-induced changes of cavity resonances. While the disorder may create a dead zone and reduce the sensitivity to rotation, it may also achieve the opposite effect and increase the sensitivity as shown recently in [48].

We note that the sensitivity of a characteristic of a microcavity resonance to rotation does not necessarily reflect the measurement sensitivity of a rotation sensor, which, in general, depends on the detection scheme that has not been discussed in this work. Nevertheless, the fundamental understanding obtained from the current study on the effect of cavity shape deformation on the sensitivity of different characteristics of a microcavity resonance to rotation will be extremely helpful for future design of a microcavity-based optical gyroscope.

Funding. Graduate Center (Graduate Center, City University of New York) (PSCCUNY 45); National Science Foundation (NSF) (ECCS-1128542, DMR-1205307).

Acknowledgment. We thank Michel Digonnet, Takahisa Harayama, and Jan Wiersig for helpful discussions.

L. G. acknowledges PSCCUNY 45 Research Grant. R. S. and H. C. acknowledge NSF support under grants ECCS-1128542 and DMR-1205307.

REFERENCES

1. R. K. Chang and A. J. Campillo, eds., "Optical processes in microcavities," in *Advanced Series in Applied Physics* (World Scientific, 1996).
2. K. J. Vahala, ed., *Optical Microcavities*, Advanced Series in Applied Physics (World Scientific, 2004).
3. S. Sunada and T. Harayama, "Sagnac effect in resonant microcavities," Phys. Rev. A **74**, 021801 (2006).
4. S. Sunada and T. Harayama, "Design of resonant microcavities: application to optical gyroscopes," Opt. Express **15**, 16245 (2007).
5. T. Harayama, S. Sunada, and T. Miyasaka, "Wave chaos in rotating optical cavities," Phys. Rev. E **76**, 016212 (2007).
6. J. Scheuer, "Direct rotation-induced intensity modulation in circular Bragg micro-lasers," Opt. Express **15**, 15053 (2007).
7. C. Peng, Z. B. Li, and A. S. Xu, "Rotation sensing based on a slow-light resonating structure with high group dispersion," Appl. Opt. **46**, 4125–4131 (2007).
8. S. Sunada, S. Tamura, K. Inagaki, and T. Harayama, "Ring-laser gyroscope without the lock-in phenomenon," Phys. Rev. A **78**, 053822 (2008).
9. M. Terrel, M. J. F. Digonnet, and S. Fan, "On the impact of slow light on coupled resonant optical waveguide gyroscope," Laser Photon. Rev. **3**, 452–465 (2009).
10. M. A. Terrel, M. J. F. Digonnet, and S. Fan, "Performance limitation of a coupled resonant optical waveguide gyroscope," J. Lightwave Technol. **27**, 47–54 (2009).
11. C. Ciminelli, F. DellOlio, C. E. Campanella, and M. N. Armenise, "Photonic technologies for angular velocity sensing," Adv. Opt. Photon. **2**, 370–404 (2010).
12. M. J. F. Digonnet, "Rotation sensitivity of gyroscopes based on distributed-coupling loop resonators," J. Lightwave Technol. **29**, 3048–3053 (2011).
13. C. Sorrentino, J. R. E. Toland, and C. P. Search, "Ultra-sensitive chip scale Sagnac gyroscope based on periodically modulated coupling of a coupled resonator optical waveguide," Opt. Express **20**, 354–363 (2012).
14. R. Sarma, H. Noh, and H. Cao, "Wavelength-scale microdisks as optical gyroscopes: a finite-difference time-domain simulation study," J. Opt. Soc. Am. B **29**, 1648–1654 (2012).
15. D. Kalantarov and C. P. Search, "Effect of input–output coupling on the sensitivity of coupled resonator optical waveguide gyroscopes," J. Opt. Soc. Am. B **30**, 377–381 (2013).
16. L. Ge, R. Sarma, and H. Cao, "Rotation-induced mode coupling in open wavelength-scale microcavities," Phys. Rev. A **90**, 013809 (2014).
17. L. Ge, R. Sarma, and H. Cao, "Rotation-induced evolution of far-field emission patterns of deformed microdisk cavities," Optica **2**, 323–328 (2015).
18. R. Sarma, L. Ge, J. Wiersig, and H. Cao, "Rotating optical microcavities with broken chiral symmetry," Phys. Rev. Lett. **114**, 053903 (2015).
19. E. J. Post, "Sagnac effect," Rev. Mod. Phys. **39**, 475–493 (1967).
20. F. Aronowitz, "The laser gyro," in *Laser Applications*, M. Ross, ed. (Academic, 1971).
21. W. W. Chow, J. Gea-Banacloche, L. M. Pedrotti, V. E. Sanders, W. Schleich, and M. O. Scully, "The ring laser gyro," Rev. Mod. Phys. **57**, 61–104 (1985).
22. J. U. Nöckel and A. D. Stone, "Ray and wave chaos in asymmetric resonant optical cavities," Nature **385**, 45–47 (1997).
23. C. Gmachl, F. Capasso, E. E. Narimanov, J. U. Nöckel, A. D. Stone, J. Faist, D. L. Sivco, and A. Y. Cho, "High-power directional emission from microlasers with chaotic resonators," Science **280**, 1556–1564 (1998).
24. B. Z. Steinberg, "Rotating photonic crystals: a medium for compact optical gyroscopes," Phys. Rev. E **71**, 056621 (2005).
25. B. Z. Steinberg, "Two-dimensional Greens function theory for the electrodynamics of a rotating medium," Phys. Rev. E **74**, 016608 (2006).
26. J. Scheuer and A. Yariv, "Sagnac effect in coupled-resonator slow-light waveguide structures," Phys. Rev. Lett. **96**, 053901 (2006).
27. B. Z. Steinberg and A. Boag, "Splitting of microcavity degenerate modes in rotating photonic crystals the miniature optical gyroscopes," J. Opt. Soc. Am. B **24**, 142–151 (2007).
28. C. Peng, R. Hui, X. Luo, Z. Li, and A. Xu, "Finite-difference time-domain algorithm for modeling Sagnac effect in rotating optical elements," Opt. Express **16**, 5227–5240 (2008).
29. D. Hah and D. Zhang, "Analysis of resonant optical gyroscopes with two input/output waveguides," Opt. Express **18**, 18200 (2010).
30. R. Novitski, J. Scheuer, and B. Z. Steinberg, "Unconditionally stable finite-difference time-domain methods for modeling the Sagnac effect," Phys. Rev. E **87**, 023303 (2013).
31. T. Shiozawa, "Phenomenological and electron-theoretical study of the electrodynamics of rotating systems," Proc. IEEE **61**, 1694–1702 (1973).
32. G. Hackenbroich, E. Narimanov, and A. D. Stone, "Quantum perturbation theory for the level splitting in billiards," Phys. Rev. E **57**, R5–R8 (1998).
33. S. A. Backers, A. P. Heberle, J. R. A. Cleaver, and K. Kler, "Shape dependence of emission from microdisk lasers," Phys. Status Solidi B **204**, 581–583 (1997).
34. H. G. L. Schwefel, N. B. Rex, H. E. Tureci, R. K. Chang, and A. D. Stone, "Dramatic shape sensitivity of directional emission patterns from similarly deformed cylindrical polymer lasers," J. Opt. Soc. Am. B **21**, 923–934 (2004).
35. S. Sunada, T. Harayama, and K. S. Ikeda, "Nonlinear whispering-gallery modes in a microellipse cavity," Opt. Lett. **29**, 718–720 (2004).
36. S. K. Kim, S. H. Kim, G. H. Kim, H. G. Park, D. J. Shin, and Y. H. Lee, "Highly directional emission from few-micron-size elliptical microdisks," Appl. Phys. Lett. **84**, 861–863 (2004).
37. J. Unterhinninghofen, J. Wiersig, and M. Hentschel, "Goos-Hanchen shift and localization of optical modes in deformed microcavities," Phys. Rev. E **78**, 016201 (2008).
38. Q. H. Song, L. Ge, A. D. Stone, H. Cao, J. Wiersig, J. B. Shim, J. Unterhinninghofen, W. Fang, and G. S. Solomon, "Directional laser emission from a wavelength-scale chaotic microcavity," Phys. Rev. Lett. **105**, 103902 (2010).
39. B. Redding, L. Ge, Q. Song, J. Wiersig, G. S. Solomon, and H. Cao, "Local chirality of optical resonances in ultrasmall resonators," Phys. Rev. Lett. **108**, 253902 (2012).
40. B. Redding, L. Ge, G. S. Solomon, and H. Cao, "Directional waveguide coupling from a wavelength-scale deformed microdisk laser," Appl. Phys. Lett. **100**, 061125 (2012).
41. Q. H. Song, L. Ge, J. Wiersig, J. B. Shim, J. Unterhinninghofen, A. Eberspacher, W. Fang, G. S. Solomon, and H. Cao, "Wavelength-scale deformed microdisk lasers," Phys. Rev. A **84**, 063843 (2011).
42. M. Hentschel, H. Schomerus, and R. Schubert, "Husimi functions at dielectric interfaces: Inside-outside duality for optical systems and beyond," Europhys. Lett. **62**, 636–642 (2003).
43. H. E. Tureci, H. G. L. Schwefel, P. Jacquod, and A. D. Stone, *Progress in Optics*, E. Wolf, ed. (Elsevier, 2005), Chap. 2, Vol. **47**.
44. E. E. Narimanov, G. Hackenbroich, P. Jacquod, and A. D. Stone, "Semiclassical theory of the emission properties of wave-chaotic resonant cavities," Phys. Rev. Lett. **83**, 4991–4994 (1999).
45. S. Shinohara, T. Harayama, T. Fukushima, M. Hentschel, T. Sasaki, and E. E. Narimanov, "Chaos-assisted directional light emission from microcavity lasers," Phys. Rev. Lett. **104**, 163902 (2010).
46. O. Bohigas, S. Tomsovic, and D. Ullmo, "Manifestations of classical phase space structures in quantum mechanics," Phys. Rep. **223**, 43–133 (1993).
47. F. Leyvraz and D. Ullmo, "The level splitting distribution in chaos-assisted tunnelling," J. Phys. A **29**, 2529–2551 (1996).
48. R. Novitski, B. Z. Steinberg, and J. Scheuer, "Finite-difference time-domain study of modulated and disordered coupled resonator optical waveguide rotation sensors," Opt. Express **22**, 23153–23163 (2014).